



# Pore Volume Characteristics of Clay-Rich Shale: Critical Insight into the Role of Clay Types, Aluminum and Silicon Concentration

Clement Afagwu<sup>1</sup> · Mohamed Mahmoud<sup>1</sup> · Saad Alafnan<sup>1</sup> · Abdullah Alqubalee<sup>1,2,3</sup> · Ammar ElHusseiny<sup>3</sup> · Shirish Patil<sup>1</sup>

Received: 26 October 2021 / Accepted: 16 February 2022 / Published online: 15 April 2022  
© King Fahd University of Petroleum & Minerals 2022

## Abstract

Shale resources contain a significant quantity of clay minerals and organic matter. These material components influence the evolution of intra- and inter-granular pore features. This study investigates the role of clay's elemental concentration, purity and types on its pore attributes. Four samples; illite, chlorite, montmorillonite, and kaolinite-rich clay samples were studied. Clay elemental composition, purity, pore shape, and structural parameters were determined. X-ray fluorescence and diffraction techniques were used to compute the elemental and mineralogical compositions of clay samples, respectively. Rock surfaces were mapped using the energy dispersive x-ray spectroscopy and scanning electron microscopy to confirm the distribution of elements and clay homogeneity, respectively in the four phyllosilicate materials. Total organic content analysis confirms the quantity of organic matter. N<sub>2</sub> adsorption/desorption experiment at 77 K and over a relative pressure range up to 0.995 was executed with a surface area and porosity analyzer, to extract information regarding the pore shape, and determine the pore volume and specific surface area. The interrelation of the purity and computed pore structure properties was established. Mineralogy and elemental analyses showed that the studied samples with clay purities of 60–98% have a combined 80–96 wt.% of Aluminum (Al), Silicon (Si), and Iron (Fe). The adsorption–desorption curve at  $p/p^o < 0.04$  and carbon content analysis indicate that clays accommodate negligible micropores. The type III and IV isotherms combined with H1, H2, and H3 hysteresis loop implied that clay had connected complex pores with plate-like, uniform cylindrical, and inkbottle shapes. Capillary condensation and evaporation curves revealed more mesopores and macropores of 2–50 nm and > 50 nm, respectively. The pore distribution plateaued around an average of 100 nm, which confirmed the suitability of the Barrett-Joyner-Halenda technique to characterize clay mesopores. Kaolinite has the highest capacity (74.43 cm<sup>3</sup>/g) to host N<sub>2</sub> gas at a standard temperature and pressure followed by montmorillonite (65.08 cm<sup>3</sup>/g), chlorite (21.01 cm<sup>3</sup>/g) and illite (16.59 cm<sup>3</sup>/g) in that order. The capacity of the pores to store fluid and their average size follow a similar pattern and increase with aluminum and clay contents. A specific surface area of the non-micropores is directly related to silicon concentration. The study provides an insight regarding the potential of kaolinite (with the highest aluminum concentration of 39.5 wt.%) as a good catalytic material required to speed up the esterification reaction. In addition, it can serve as a waste repository and a material for the treatment of phosphorus-containing contaminants in polluted areas. This research confirms that montmorillonite with the largest specific surface area in non-micropores and silicon content of 63.9 wt.% promotes reactivity and cation exchange interaction. However, this high basal spacing attribute of the material means that swelling will occur in the presence of water.

**Keywords** Pore volume characteristics · Clay-rich shale · Mineralogy · Clay minerals, aluminum and silicon

✉ Mohamed Mahmoud  
mmahmoud@kfupm.edu.sa

<sup>1</sup> Petroleum Engineering Department, College of Petroleum Engineering and Geosciences, King Fahd University of Petroleum and Minerals (Eastern Province), Dhahran 31261, Saudi Arabia

<sup>2</sup> Center for Integrative Petroleum Research, College of Petroleum Engineering and Geosciences, King Fahd

University of Petroleum and Minerals, Dhahran 31261, Saudi Arabia

<sup>3</sup> Geosciences Department, College of Petroleum Engineering and Geosciences, King Fahd University of Petroleum and Minerals, Dhahran 31261, Saudi Arabia



## List of Symbols

$A_m = 0.162 \text{ nm}^2$	Is nitrogen molecule surface area at 77 K
$c_{\text{BET}}$	BET isotherm fitting constant
$N_A$	Avogadro's number ( $6.022 \times 10^{22} \frac{\text{number}}{\text{mol}}$ )
$p^o$	Standard pressure of $\text{N}_2$ gas $\sim 1.02$ bar at 77.4 K
$p/p^o$	Relative pressure of $\text{N}_2$ gas between 0.001 and 0.995 and 77.4 K
$r$	Pore radius (m)
$R = 8.314 \text{ J/Kmol}$	Is universal gas constant
$S_{\text{BET}}$	Total specific surface area ( $\text{m}^2/\text{g}$ )
$S_{\text{ext}}$	Non-micropores specific surface area
$S_{\text{mic}}$	Micropores specific surface area
$t_{\text{ads}}$	Statistical thickness of adsorbed layer ( $\text{\AA}$ )
$T$	Temperature (K)
$V_{\text{ads}}$	Total volume of adsorbed $\text{N}_2$ gas at $p/p^o = 0.001$ – $0.995$ and 77.4 K ( $\text{m}^3/\text{kg}$ )
$V_m$	Monolayer adsorption capacity ( $\text{cm}^3/\text{g}$ )
$V_{\text{mic}}$	Micropore filling volume
$V_{\text{mol}}$	Molar volume ( $\text{m}^3/\text{mol}$ )
$\alpha$	Shape factor of the gas/liquid interface during adsorption
$\Delta H_m$	Heat of gas condensation
$\gamma$	Surface tension of liquid nitrogen ( $\text{N/m}$ )

## Abbreviations

AFM	Atomic force microscopy
APM	Areal porosity method
BET	Brunauer, Emmett and Teller
BJH	Barrett, Joyner and Halenda
BSE	Backscatter electron
DRIFTS	Diffuse reflectance Fourier transform infrared spectroscopy
EBS	Electron backscatter diffraction
EDX	Energy-dispersive X-Ray spectroscopy
EGME	Ethylene glycol monoethyl ether
HPCP	Hierarchical clustering of principal components
IUPAC	International union of pure and applied chemistry
LEED	Low energy electron diffraction
LOD	Limit of detection
MIP	Mercury injection porosimetry
NDIR	Non-destructive infrared
NMR	Nuclei magnetic resonance

QEMSCAN	Quantitative evaluation of minerals by scanning electron microscopy
SANS	Small angle neutron scattering
SAXS	Small angle X-ray scattering
SEM	Scanning electron microscopy
SSA	Specific Surface Area
SSM	Solid sample measurements
STP	Standard temperature and pressure
3D-SIMS	Three-dimensional secondary ion mass spectroscopy
TEM	Transmission electron microscopy
TOC	Total organic content
XRD	X-ray diffraction
$\mu\text{XRF}$	Micro- X-ray fluorescence

## 1 Introduction

Clay minerals can exist in both a free state and as components of inorganic minerals present in shale reservoirs [1–3]. These phyllosilicate materials possess sufficient surface area and void spaces for fluid storage in compressed and sorbed phases depending on their chemical composition [4, 5]. International Union of Pure and Applied Chemistry (IUPAC) classified the pores sizes in porous media into three basic categories such as; micropores (< 2 nm), mesopores (2–50 nm), and macropores (> 50 nm) [6, 7]. The IUPAC grouping will be used throughout this article. X-ray Powder Diffraction (XRD) and X-ray Fluorescence (XRF) techniques are widely used to identify the minerals in clay [8, 9]. Srodon [10] employed XRD and XRF analyses to identify and quantify clay minerals in pure and clay-containing rocks. Similarly, Mattioli et al. [11] studied the 15 mixed and rich samples of illite, chlorite, smectite and kaolinite clay with the same techniques to understand the suitability of its mineralogy and chemical composition for cosmetic applications. Nevertheless, the semi-quantitative data from such methods do not discriminate between the main phases of the identified minerals at a much higher resolution. Further insights into the chemical constituents and physical features of clay are generally possible using other methods based on the principles of radiation and penetrating-fluids.

There are many applications for some common radiation-driven methods such as scanning electron microscopy (SEM), transmission electron microscopy (TEM), nano- and micro-CT scanning, nuclear magnetic resonance (NMR), small-angle neutron scattering (SANS), and Small-Angle X-ray Scattering (SAXS) for pore size characterization [12–14] and fluid transport monitoring [15]. Other sets of techniques, based on the principle of penetrating fluid and have been

successfully applied to track pore distribution, Specific Surface Area (SSA), and pore spaces are carbon dioxide (CO<sub>2</sub>), Mercury Injection Porosimetry (MIP), nitrogen (N<sub>2</sub>), and argon gas adsorption [5, 16–19]. Aringhieri [16] employed an N<sub>2</sub>-adsorption experiment to investigate the distribution of 1.5–100 nm pores in four clay minerals and soil samples. Ross and Bustin [5] studied illite, montmorillonite, kaolinite and chlorite clay structure using low-pressure N<sub>2</sub> and CO<sub>2</sub> sorption techniques. Kuila [18] employed the N<sub>2</sub> adsorption technique to determine the micropores and mesopores SSA and size distribution in mixed illite–smectite, kaolinite clay and shale rock. Wang [20] studied the micropores (< 1.0 nm) in illite, montmorillonite, kaolinite, and illite–smectite mixed layers using N<sub>2</sub> and CO<sub>2</sub> low-pressure adsorption.

Meanwhile, several studies are interested in characterizing the pore structure, chemical composition and physical properties in clay by combining multiple approaches [21–25]. Hassan et al. [21] utilized both Atomic Force Microscopy (AFM) and low-pressure argon adsorption analyses to determine the SSA of non-swelling kaolinite edge face coupled with edge and basal face of illite. Chen [26] availed a coupled nano-indentation, SEM, and Energy Dispersive X-ray Spectroscopy (EDX) to study the effect of crystalline Calcium Silicate Hydrated (C–S–H) composite on the mechanical properties of cement with a low water/cement ratio. Macht [22] computed the edge and basal-specific surface area in illite and montmorillonite clay using AFM, N<sub>2</sub> gas adsorption, and Ethylene Glycol Monomethyl Ether (EGME) liquid adsorption methods. Boulingui et al. [27] characterized the mineralogy, physical and chemical of raw kaolinite and illite-rich clay using XRD, Diffuse Reflectance Fourier Transform Infrared Spectroscopy (DRIFTS) and SEM. The outcome showed that Gabon-originated clays are rich in silicate and poor in aluminum elements. Zaffar and Lu [28] integrated MIP and N<sub>2</sub> adsorption to study the pore distribution in three clayey soils. Li [29] combined SEM, focused ion beam (FIB)-SEM, areal porosity method (APM), and MIP to study the organic and inorganic porosities in mudstone and dolomite. Wilson et al. [30] employed Nano-Indentation and Quantitative EDX to study the micro-chemo-visco-mechanical properties in a heterogeneous cement paste. Elgamouz [31] studied the elemental oxides in clay and their relationship with porosity and SSA using XRD, thermal analysis, infrared spectral and SEM techniques. Kariem [23] employed integrated SEM, EDX, and XRD measurements to compute the volume fractions of these mineral phases in fired clay materials and the impact on their mechanical behavior. Qian [32] summarized the application of surface analytical techniques like low energy electron diffraction (LEED), Electron Backscatter Diffraction (EBSD), Quantitative Evaluation of Minerals by SEM (QEMSCAN), three-Dimensional Secondary Ion Mass Spectroscopy (3D-SIMS) and many others for earth science applications. In addition, some researchers

have integrated the Nuclei Magnetic Resonance (NMR) in addition to other radiation and/or penetrating fluid techniques to investigate the clay pores structure [33, 34]. Thus far, there are available experimental studies to determine the chemical composition, physical properties and porous structure of different clay types using XRD/XRF, AFM, thermal analysis, SEM, SEM–EDX, NMR, low temperature and pressure gas adsorption and other methods. However, there are limited integrated studies that investigate the role of clay chemical composition and mineralogy on the development of intra-granular pore volumes attributes in clay-rich shale. It is notable that the role of kerogen types and maturity [35–38] on the pore development of organic-rich shale has been studied in detail compared to clay-containing unconventional reservoirs. The insights in the establishment of the connection between the pore structure properties, clay types and elemental analysis will advance the development of synthetic clay materials with specific chemical compositions for improved repositories and surface reactivity applications.

In this study, the role of purity and elements contained in clays on their pore structural properties was investigated. The four clay types utilized for the research are kaolinite, montmorillonite, chlorite and illite. Clay elemental concentrations and purity were computed with Micro-XRF ( $\mu$ XRF) and XRD, and confirmed using image maps from XDS and SEM, respectively. A low-temperature N<sub>2</sub> adsorption/desorption experiment was performed at 77 K and over a relative pressure range up to 0.995. Pore shape was inferred from the hysteresis loop and isotherm type.

Furthermore, the interrelation between the clay purity, elemental concentration, specific surface area and pore volume at different pore-scale was established. This article was outlined as follows: Sect. 2 provides the detail of the materials and methods utilized for this study such as,  $\mu$ XRF, XRD, organic content analysis, SEM–EDX in addition to low-pressure adsorption using nitrogen probes. Section 3 presents the mineral composition and clay purity results and discusses how these concentrations relate to the average pore size, pore volume, and specific surface area of studied clays. Section 4 discusses the implications of using aluminum and silica-rich clay in waste management and reaction processes. Finally, Sect. 5 concludes this research with insight into future research focus.

## 2 Materials and Methods

This study utilized four outcrops' samples of clay-rich rocks with different degrees of purity, obtained from a vendor in the United States of America. The four samples include montmorillonite, kaolinite, chlorite and illite. All samples have been pulverized with a mortar and pestle to improve the surface area responsible for the interactions between fluid and



rock. Crushed clay is widely used in the literature in adsorption studies and for XRD analysis [39, 40]. The phyllosilicate materials were granulated in such a way as to maintain a relatively large grain, with a mean diameter that is less than 250  $\mu\text{m}$  to prevent inter-particle nanoporosity from forming among the clay grains. The chemical composition and mineralogical of the studied clay samples were determined using  $\mu\text{XRF}$  and XRD techniques, respectively. The distinction between these samples was mapped using SEM–EDX of QEMSCAN 650F. JEOL JCM-7000 NeoScope Benchtop SEM was used to image the variation in the purity of the studied samples at 200  $\mu\text{m}$  resolution. Organic content analysis was performed on kaolinite, montmorillonite, illite and chlorite-rich rocks. Surface area and porosity analyzer were utilized to conduct  $\text{N}_2$  adsorption/desorption experiments at 77.4 K and over a range of relative pressure up to 0.995. The experiments will be described in detail afterward.

### 2.1 $\mu\text{XRF}$ Analysis

Brucker M4-Tornado  $\mu\text{XRF}$  instrument was utilized to determine the elements and oxides present in the clay materials. The equipment contains a rhodium source with voltage and current of 50 kV and 600  $\mu\text{A}$ , respectively. In addition, the device has a polycapillary optic that is around 20  $\mu\text{m}$  spot-size and two silicon drift detectors. Five spots were selected randomly per sample to ensure reproducibility. Then, the samples were scanned with a high-energy X-ray, followed by the emission of a characteristic fluorescent X-ray. The secondary rays emitted afterward were examined with the Module M-Quant available in the M4 software package. This software provides dependable results of the bulk samples' composition, because it is based on the fundamental parameters models that use less standard analysis. Results were presented as normalized percentages of the elemental concentration.

### 2.2 XRD Analysis

Malvern PANalytical Empyrean was used to identify and quantify the mineralogical phases of the studied samples. After pulverizing the samples, this XRD instrument collected the phase peaks, which have been spotted and measured using the Highscore plus of PANalytical™ attached with ICCD PDF-4+2022. Phase concentration was estimated by summing the XRD in automated full pattern summation mode. The alignment or maximum shift was set at  $0.3^\circ$ . A Limit of detection, set at 1.0 wt.% was utilized during the fitting process to evaluate the phase-detection limits. At the same time, the reference patterns that are below the lowest concentration were eliminated.

### 2.3 SEM–EDX and SEM Analyses

SEM–EDX of QEMSCAN 650 F was deployed to map the elemental concentration in the clay samples. This instrument operates on the SEM principles and is attached with two Bruker EDX detectors. The capability and applications of QEMSCAN 650F are present in the literature [41]. Before SEM–EDX scanning, the same samples used for  $\mu\text{XRF}$  and XRD analyses were compressed and coated with platinum. The SEM backscatter electron (BSE) images and EDX mapping were generated at 15 kV with a 13 mm working distance.

The compressed studied samples coated with platinum were scanned via JEOL JCM-7000 NeoScope Benchtop SEM. This technique was run on 15 kV and 12 working distances to scan all the sampled surfaces.

### 2.4 Total Organic Content (TOC) Analysis

Carbon-containing rocks host significant micropores that could impact clay pore size distribution. A detailed examination of clay micropore distribution will not be required if the TOC < 1wt.% [42]. TOC analysis was performed to determine the extent of the presence or absence of carbon compounds in the studied clay samples. This inspection employs the principle of aerobic combustion of organic compounds using a catalyst to produce  $\text{CO}_2$ . A direct non-dispersive infrared detection was utilized to determine the produced carbon dioxide. Approximately 200 mg of homogenized and dried clay samples were weighed and placed into a pre-combusted and clean carbon-free ceramic boat. Afterward, the samples were treated with a small volume of concentrated hydrochloric acid and at least 2 h were allowed to remove the inorganic carbon from the sample completely. Before the boats containing the inorganic carbon-free samples were placed on Shimadzu SSM 5000A assembly and combusted at  $900^\circ\text{C}$  in a stream of  $\text{O}_2$  gas, they were dried on a hot plate at  $105^\circ\text{C}$ . Finally, a TOC-VCPH carbon analyzer equipped with a non-destructive Infrared (NDIR) detector was used to measure the produced  $\text{CO}_2$  for each sample.

### 2.5 Low-Pressure $\text{N}_2$ Adsorption

Micromeritics ASAP 2020, an automatic surface area and pore size analyzer was used for the measurements. Each clay sample used was crushed to < 250  $\mu\text{m}$  (about 60-mesh number). It is worthy to note that the surface area of grain utilized for this analysis is at a scale where there is a negligible effect of sedimentary or macro fabrics on the clays' sorption capacity [5, 18]. First, a dried and empty sample tube that contains a filler rod and seal frit was weighed in an analytical balance. The second step was to weigh and record an appropriate sample ranging from 0.20 to 0.35 g.



Furthermore, the sample was added to the empty tube and the new weight was recorded. The same procedure was used for the other three samples. The clay materials were degassed under vacuum for 80 min at 220 °C. The weight employed for analysis is the difference in sample weight before and after degassing. After that, the sample analysis proceeded, and N<sub>2</sub> adsorption and desorption branch measurements were accomplished at 77.4 K, between  $p \sim 0.001p^o$  and  $p \sim 0.995p^o$ . Brunauer-Emmet-Teller (BET) equation, Barrett-Joyner-Halenda (BJH) based on Kelvin equation, and Harkins and Jura t-plot method were used to determining the SSA, pore distribution at various pore-scales, and micropores properties, respectively. The theoretical foundation of these constant temperature models will be expounded in the subsequent subsections.

### 2.5.1 Brunauer–Emmett–Teller (BET) Equation

BET is a multilayer adsorption model that describes the distinct energy of different adsorption sites. This isotherm equation that is employed to compute the total SSA of mesoporous to microporous materials [43] is as follows:

$$V_{ads} = V_m \frac{c_{BET}(p/p^o)}{(1 - p/p^o)(1 + (c_{BET} - 1)p/p^o)} \tag{1}$$

where  $V_m$  is monolayer adsorption capacity (cm<sup>3</sup>/g),  $p/p^o$  is the relative pressure of nitrogen gas at a given pressure and temperature.  $c_{BET} = \exp((\Delta H_1 - \Delta H_m)/RT)$  is constant,  $\Delta H_1$ , is the heat of adsorption (J/mol),  $\Delta H_m$ , is the heat of gas condensation,  $R = 8.314$  J/Kmol is a universal gas constant,  $T$  is the temperature (K). Then,  $s_{BET} = V_m V_{std} N_A A_m$ , is total specific surface area (m<sup>2</sup>/g), where, ( $N_A = 6.022 \times 10^{22}$  number/mol),  $A_m = 0.162\text{nm}^2$  is the surface area of nitrogen molecules at 77 K [44], and  $V_{std} = 22.4 \times 10^3$  cm<sup>3</sup>/mol of gas at STP. It is important to state that the model is valid for  $0.05 < p/p^o < 0.35$ . To avoid a complex model fitting procedure, the original BET Eq. (1) is re-written in a linear form [45, 46] as:

$$\frac{p/p^o}{V_{ads} \cdot (1 - p/p^o)} = \frac{1}{V_m \cdot c_{BET}} + \frac{c_{BET} - 1}{V_m \cdot c_{BET}} \cdot \frac{p}{p^o} \tag{2}$$

where the slope and the intercept of the plot of  $\frac{p/p^o}{V_{ads} \cdot (1 - p/p^o)}$  versus  $\frac{p}{p^o}$  are utilized to compute  $V_m$  and  $c_{BET}$ , respectively. To guide the selection of  $p/p^o$  fitting range, which should not be the same for all materials, the criteria suggested by Rouquerol et al. [47] must hold. First the  $c_{BET}$  must be positive. Second, the BET-plot intercept is positive, and the term  $V_{ads}(p^o - p)$  should continuously increase with  $p/p^o$ . Otherwise, if the conditions fail, the relative pressure range should be narrowed, while the fitting is repeated. It is

worthy to note that the monolayer adsorption parameter overestimate the micropores volume by accounting for not only the adsorbate filled in the micropores but also the content of the statistical monolayer in the non-micropores [47].

### 2.5.2 Harkins and Jura t-Plot Model

‘t-plot’ is one of the models utilized to compute micropores volume and specific surface area in a material. It captures the amount of fluid that could be contained in supermicropores and some ultramicropores within 0.4–2.0 nm [46], and is represented as a graph of adsorbed volume ( $V_{ads}$ ) versus a statistical thickness ( $t_{ads}$ ) of the adsorbed layer (angstrom). The presence of these pore categories in this material will be confirmed from TOC analysis, so that any need for micropores characterization using more advanced techniques will be justified. More importantly, there are several developed models to estimate  $t_{ads}$ . However, the Harkins and Jura thickness equation, which is the most widely applied for N<sub>2</sub> adsorption [48] was utilized in this study.

$$t_{ads} = \left[ \frac{13.99}{0.034 - \log(p/p^o)} \right]^{1/2} \tag{3}$$

Interestingly, a t-plot for a material that hosts a negligible amount of micropores will produce a straight line that passes through the point (0, 0) of the graph. Conversely, a micropores-containing material shows a straight line and a concave-down curve at medium and lower  $t_{ads}$  values, respectively. Meanwhile, a convex up deviation from the linear trend at higher  $t_{ads}$  indicates capillary condensation in mesopores. The slope  $m_{tplot}$  and intercept  $b_{tplot}$  of the straight-line portion at the medium of  $t_{ads}$  were employed to compute the external specific surface area,  $S_{ext} = 15.47m_{tplot}(\text{m}^2/\text{g})$  and micropores volume of adsorbed gas,  $V_{mic} = 0.001547b_{tplot}(\text{cm}^3/\text{g})$ , respectively. Finally, the micropores SSA,  $S_{mic} = s_{BET} - S_{ext}$ , and  $s_{BET}$  is the total SSA ( $s_{BET}$ ) while,  $S_{ext}$  is the non-micropores SSA [18, 46].

### 2.5.3 Barrett-Joyner-Halenda (BJH) Equation

BJH method mainly characterizes the pore distribution in mesoporous materials, and is based on Kelvin equations in cylindrical pores. Pore size distribution computed with this model is possible by analyzing the capillary condensation phenomenon in the net pore space after discounting  $t_{ads}$  from pore radius,  $r$ .

$$\ln(p/p^o) = -\frac{\alpha \gamma V_{mol}}{RT(r - t_{ads})} \tag{4}$$

where  $\alpha$  is the shape factor of the gas/liquid interface during the adsorption process. Assumption of  $\alpha = 1$  is made in

**Table 1** Micro-XRF elemental composition in the four studied samples

Clay types/elements	Al	Si	S	K	Ca	Ti	Mn	Fe	Mg	Na	Others
Illite	14.73	55.50	0.02	13.65	2.67	1.50	0.09	9.94	1.64	0.00	0.25
Chlorite	22.99	42.05	2.16	6.16	0.39	1.78	0.12	22.26	1.68	0.00	0.40
Kaolinite	39.49	55.67	0.01	0.00	0.10	3.44	0.01	0.80	0.00	0.00	0.47
Montmorillonite	17.89	63.90	0.51	0.94	2.29	0.26	0.10	10.74	1.91	1.31	0.14

the interpretation of the pore distribution with this method, and it signifies that the interface has a cylindrical shape [49],  $\gamma$  is the surface tension of liquid nitrogen (N/m),  $V_{\text{mol}}$  is molar volume ( $\text{m}^3/\text{mol}$ ),  $r$  is pore radius (m). The shape factor also denotes the topology and influences the interpretation of the capillary condensation phenomenon. Depending on the assumptions, the adsorption–desorption hysteresis loop could be asymmetrical (ellipsoidal) for the pores with constrictions and symmetrical for regular cylindrical pores [49] because of condensation pressure difference for the two cases. Kelvin-based model (Eq. 4) could underestimate the pore volume in a material with almost 20–30% of micropores because pore shape is usually asymmetric in small pores. However, in mesopores- and macropores-dominated structures, the consequences of this phenomenon will be negligible. The results of the elemental and mineralogy analysis coupled with low-pressure adsorption/desorption studies will be presented in the results section. Integration of the clay purity, the concentration of dominant elements and adsorption information will provide further insights into the storage capacity in clay mineral grains and its associated properties such as pore shapes complexity, pore volume and SSA at multiscale.

## 3 Results and Discussions

### 3.1 Sample Characterization

The elemental concentration, clay purity and surface mapping of elements obtained from the  $\mu\text{XRF}$ , XRD and SEM–EDX, respectively are summarized in this section. The first subsection presents the elemental composition results from  $\mu\text{XRF}$ . Furthermore, the X-ray diffraction results from which the main minerals in the sample are identified by the peak positions and with reference to an established literature library are made available in the second subsection. The outcome of the TOC analysis and mineralogy summary is also presented in tabular form. In the final subsection, SEM–EDX surface maps show the distribution of elements in the studied clay samples.

#### 3.1.1 Elemental Composition of $\mu\text{XRF}$

Both Table 1 and Fig. 1a shows the elemental concentration of  $\mu\text{XRF}$  in each clay-rich sample. The non-destructive analytical technique showed a significant quantity of aluminum and silicon in the four clay samples. It is obvious from the same figure that there is a great contribution of aluminum and silicon wt.% compared to Titanium, Potassium, Calcium, Manganese, Iron, Sulfur, Magnesium and Sodium elements in clay. Si, Al and Fe, are the major sandstone components, and account for over 80–96% of the studied clay samples. The silicon high content provides the first hint that the materials will contain macropores, commonly associated with the Silica found in quartz-rich rocks. The aluminum content is fairly related to the clay purity in wt.% (Fig. 1b). In other words, irrespective of the clay type, increase in clay purity implies a higher aluminum concentration.

#### 3.1.2 XRD Mineralogy and TOC Analyses

XRD mineralogical analysis in Fig. 2 means that clay minerals are present in the samples of kaolinite, montmorillonite, chlorite and illite. From the XRD data, the montmorillonite sample has an average purity of 92.1% with traces of quartz (av. 7.9%) and vermiculite clay minerals (av. 2.3%). The kaolinite sample has an average of 97.2% purity, and a very small amount of calcite (av. 2.2%) and strontianite minerals (av. 0.6%). On the other hand, chlorite does not only contain chlorite clay minerals (avg. 94%) but also minor fractions of anorthoclase (av. 5.4%), pyrite (av. 0.5%) and quartz minerals (av. 0.1%). Furthermore, illite average purity is 58.9%, quartz (15.7%) and chlorite clay (6%). In the four samples, clay crystalline materials account for about 58.9–97.2% weight. The TOCs of the four samples, ranging from less than 0.005% to 0.76%, are generally low, implying that there are negligible amounts of micropores, which are usually associated with the organic matter constituents. For this reason, no further analysis will be required to uncover the amount of intra-granular micropores in this study. Table 2 presents the TOC analysis results and clay purity wt.% of the four samples obtained from XRD.

**Fig. 1 a** Elemental composition by clay types, **b** relationship between clay wt. % from XRD and aluminum wt. % from  $\mu$ XRF for chlorite, illite, kaolinite and montmorillonite-containing clay samples

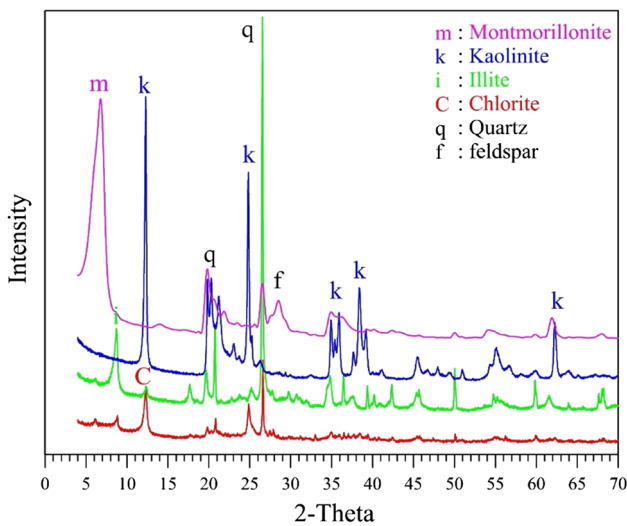
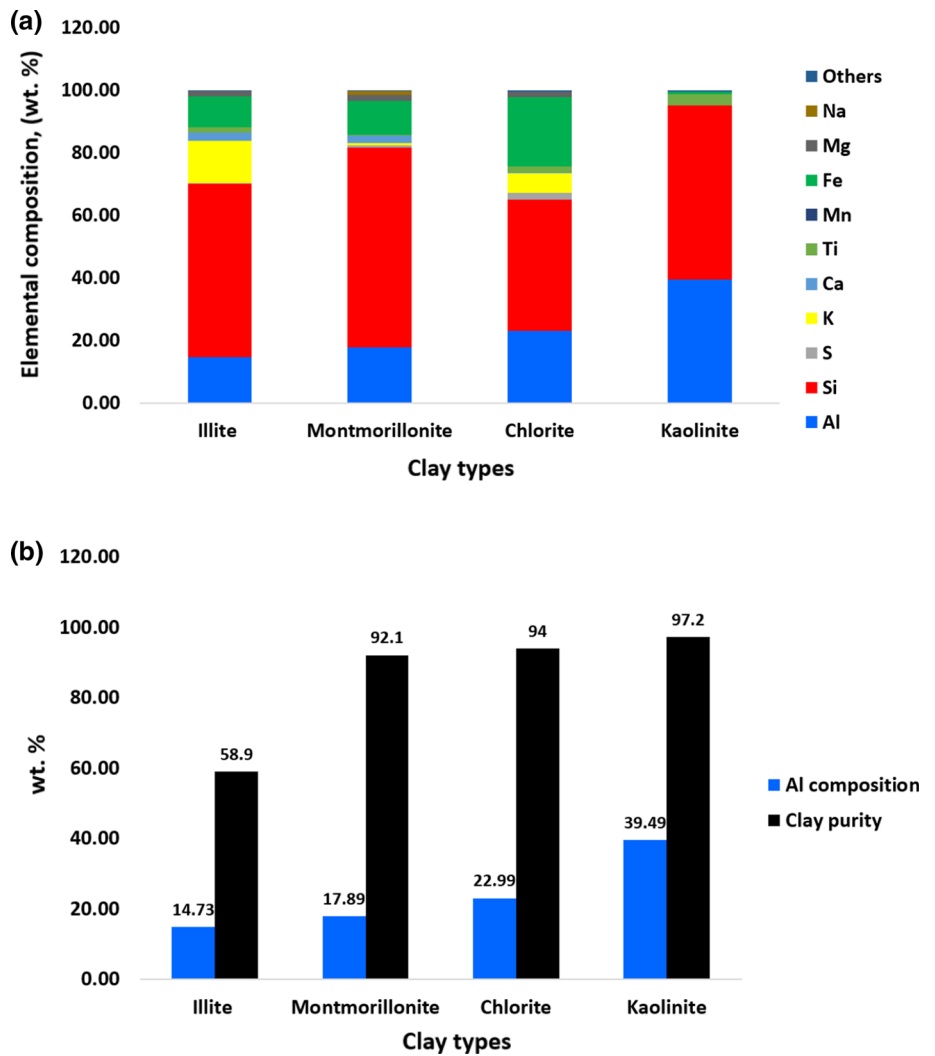


**Fig. 2** XRD patterns from montmorillonite, kaolinite, illite and chlorite-rich samples

**Table 2** TOC and clay purity from organic content and XRD analysis

Sample ID	TOC, wt. %	Clay purity, wt. %	Others, wt. %
Illite	0.005	58.9	41.1
Montmorillonite	0.010	92.1	7.9
Chlorite	0.750	94	6
Kaolinite	0.760	97.2	2.8

### 3.1.3 SEM–EDX Surface Elemental Mapping

Figure 3 depicts the images of the major elements in the clay samples such as silicon, aluminum, iron, and others contained in the studied clay samples. The dispersive x-ray spectroscopy map is a better representation of the elemental compositions in kaolinite, chlorite, montmorillonite and Illite samples. The blue color signifies aluminum and confirms the results from  $\mu$ XRF analysis (Table 1), that the aluminum

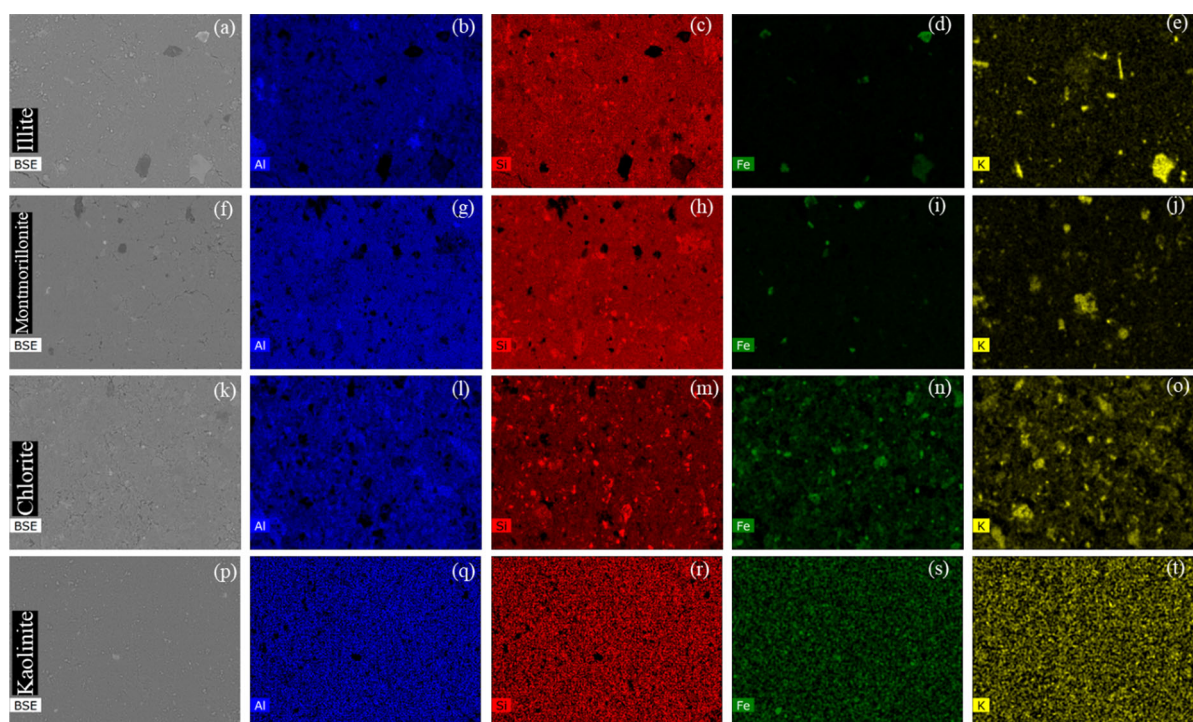


**Fig. 3** Images from SEM–EDX showing aluminum (Al), silicon (Si), iron (Fe) and potassium (K) in clay minerals: **a–e** illite and **f–j** montmorillonite, **k–o** chlorite and **p–t** kaolinite samples

concentration is the highest in kaolinite, followed by chlorite, montmorillonite, and the least in the illite clay sample. Similarly, the silicon content representing the deepest red is the highest in montmorillonite, followed by kaolinite and illite, and the least in chlorite (Table 1).

### 3.2 Morphological Characteristics Using SEM

SEM images present the morphology of the studied clay samples in Fig. 4. The purpose of the mapping of the surface is to show the material form, shape and structure. It is interesting that kaolinite is more homogeneous and confirms the mineralogy results of the individual purity. Kaolinite clay has the highest purity of 97.2% according to Table 2. In the same way, the pore shapes may be challenging to infer from a 200  $\mu\text{m}$  resolution of surface imaging. Thus, a more detailed mapping of higher resolution will be required. However, the current study is limited by the absence of solid samples for all the clay samples under consideration. An alternative means of using compressed pulverized material is utilized for this analysis (detailed in Sect. 2). The dark features in Fig. 4 may represent artifacts like pores, carbon content or any other feature, which will require further analysis to confirm. More importantly, detailed information regarding the physical properties of clay structures like pore shapes will be determined from the adsorption–desorption data.

### 3.3 Low-Pressure $\text{N}_2$ Isothermal Measurements

Isotherms' behavior depends on the pore morphology and degree of interactions between the adsorbent and adsorbate system. In other words, the adsorbate-adsorbent system, pore-size scale and storage mechanisms are inter-related. In micropores, for instance, micropores filling is the controlling process, while capillary condensation and multilayer adsorption are prevalent mechanisms in mesopores and macropores respectively [18]. In the adsorption–desorption curve, a reversible path occurs in  $< 2.0$  nm pores filling process at a very low relative pressure. However, at a higher relative pressure  $p/p^o$ , capillary condensation and desorption occurs mainly in the 2–50 nm pores. At this stage, if a limiting adsorption or plateau is observed, this indicates a complete mesopores filling. Contrary to the behavior in the available mesopores, the macropores in the materials will exhibit a complete reversible isotherm. More description of the pore shape complexity, pore size, specific surface area, and volume can be obtained from the constant temperature measurement [17–19]. According to the IUPAC classification, the six types of adsorption isotherms and four types of hysteresis loops, available to characterize the physisorption mechanisms of porous solids are I to VI [18, 19] and H1 to H4 [50] respectively. Nitrogen adsorption and desorption curves at STP for the different clay-rich samples in this study are presented in Fig. 5. Based on these groupings, the measured adsorption isotherms depict a combination of type III



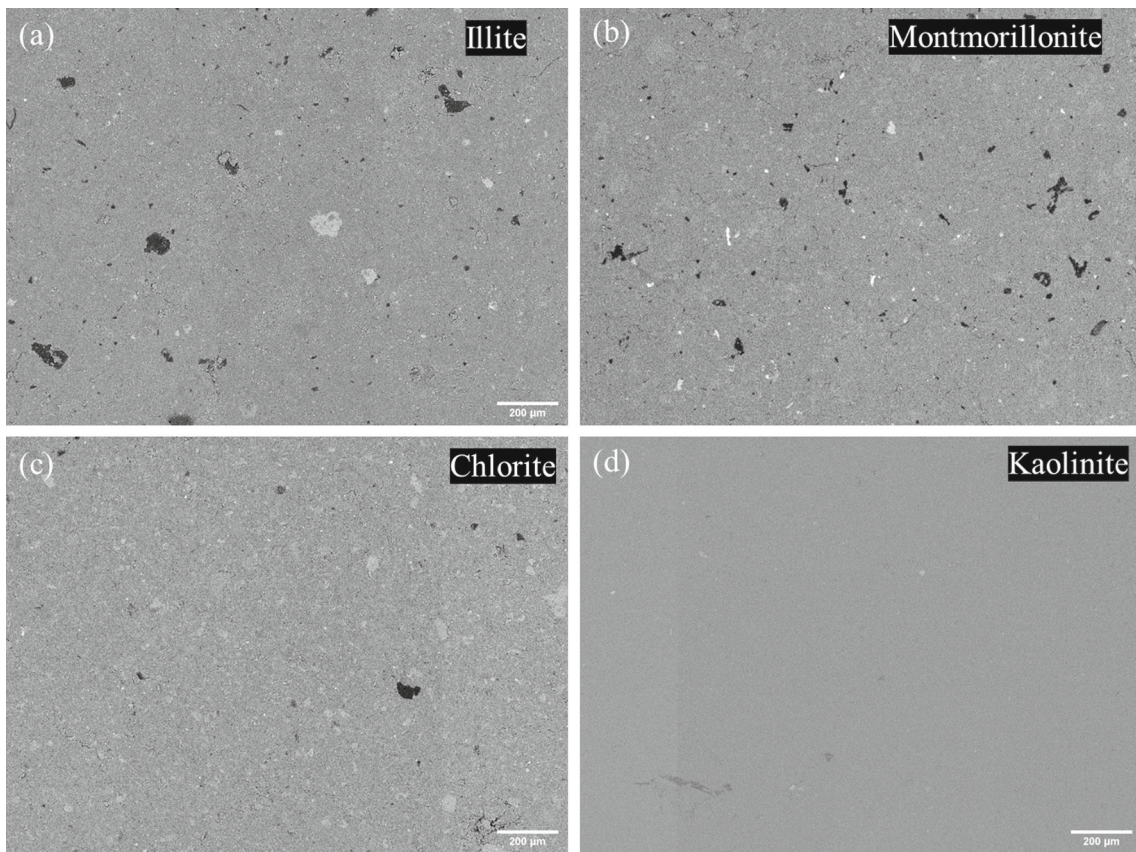


**Fig. 4** SEM images of L to R **a** illite and **b** montmorillonite, **c** chlorite and **d** kaolinite samples showing vividly the degree of homogeneity of the clay materials

**Fig. 5** The N<sub>2</sub> adsorption and desorption plots at standard temperature and pressure (STP) **a** chlorite, **b** illite, **c** kaolinite and **d** montmorillonite rich samples

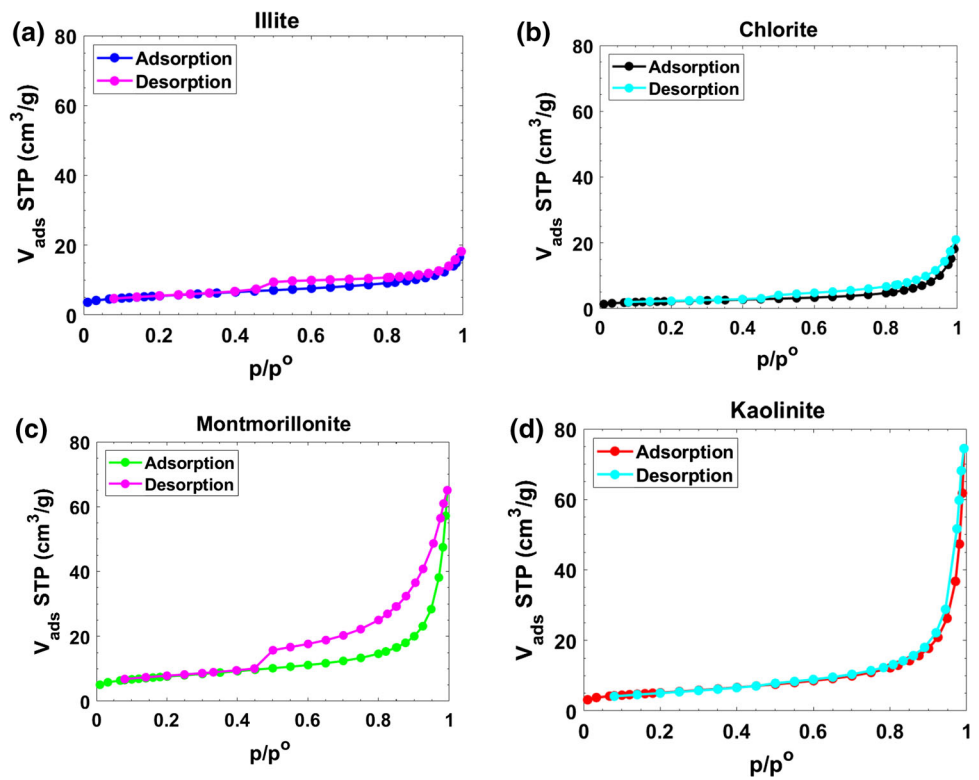
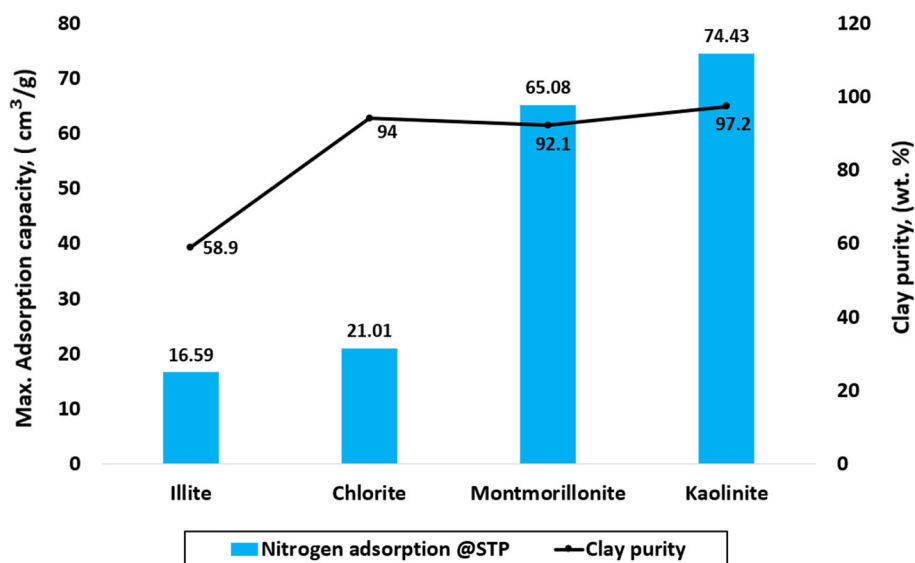


**Fig. 6** The relationship between maximum adsorption capacity at STP ( $p/p^o = 0.995$ ) and clay purity



and IV type, and are observed in the relative low-pressure and intermediate-to-high pressure range respectively [50]. The isotherm types suggest that there is a negligible quantity of micropores and a significant amount of mesopores in the clay samples respectively. In other words, the property of type IV is the hysteresis loop, which confirms the presence of mesopores in the clay samples studied. While type III is characterized by a very small amount of microporous materials with negligible adsorption amount at relatively low-pressure region  $p/p^o < 0.04$ . Besides, the organic content analysis showed that the phyllosilicate material has a TOC below 1%, and insinuates that the micropores usually present in organic matter is negligible. There is a steady increase in the adsorption amount after the very slight micropores filling, and this reflects the stage of completing monolayer adsorption. Then, the multilayer adsorption process is about to commence. Capillary condensation of N<sub>2</sub> is the final mechanism in the mesopores, and represents the filling of the mesopores above 0.9 relative pressure (Fig. 5a–d). Nevertheless, no plateau was observed even at the experimental relative pressure of 0.995, and this suggests an incomplete multilayer adsorption in the large pores (macropores). At a relative pressure of  $p/p^o \sim 0.994$ , kaolinite hosts the highest nitrogen adsorption capacity at STP (74.43 cm<sup>3</sup>/g) followed by montmorillonite (65.08 cm<sup>3</sup>/g), chlorite (21.01 cm<sup>3</sup>/g) and least in illite (16.59 cm<sup>3</sup>/g) (Fig. 6). Notably, there is a relationship between the total adsorption capacity and the clay purity wt.%.

Conversely, the desorption process starts from the macropores as pressure declines. Interestingly, a gap was observed between the adsorption and desorption path in the 2–50 nm pores region. The space between the evaporation and condensation phase in the mesopores is called the hysteresis loop. Again, the loop existing at high relative pressure supports

the type IV adsorption isotherm class, and the size of the envelope could infer the degree of 2–50 nm pores present in the clay. Interestingly, this observation is consistent with the adsorption–desorption study on clay minerals in the literature [20, 51]. Several reasons that explain the occurrence of hysteresis include but are not limited to pore-blocking effects, deformation of adsorbent, metastability of adsorbate and adsorbate molecular chain length and so on. This pore-blocking process by the mesopores could provide a good reason for the absence of capillary evaporation in some large pores. Precisely, the condensation pressure in larger pores is higher than in small pores, which creates a prevention of capillary evaporation from large pores by the liquid nitrogen in the connected small pores. The small pores are required to be emptied before desorption can take place in those macropores compartments. The adsorption curve provides information regarding the pore size distribution and rock properties.

Meanwhile, the desorption and hysteresis loops tell the pore-blocking phenomenon [52]. From Fig. 5a, the illite shows a smaller and asymmetric hysteresis loop of type H2 with a relatively less steep desorption branch, and hints at inkbottle-shaped pores' dominance. In addition, the absence of an obvious limiting adsorption at high relative pressure suggests the presence of some type of H3 slit-shaped pores and/or macropores. A similar pattern was observed in the chlorite (Fig. 5b). It contains the same degree of hysteresis loop as illite, which means that the two samples may contain relatively equal amounts of mesopores.

Contrariwise, the montmorillonite depicts a wide and asymmetric loop in Fig. 5c, of type H2 with a steep desorption branch, and could hint that the rock contains mainly inkbottle-shaped pores and more mesopores. Besides, there is no horizontal peak at high relative pressure. The absence of adsorption plateau similarly insinuates the presence of

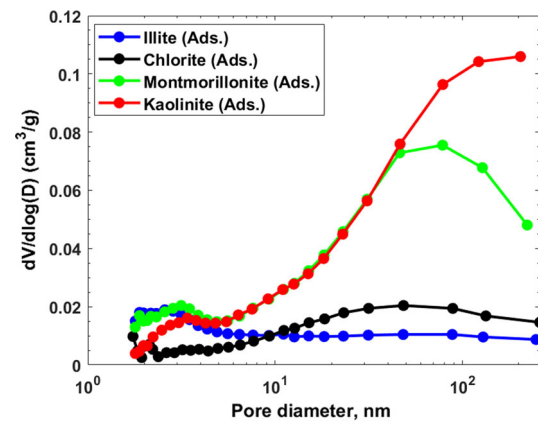
some type H3 plate-like pores and/or macropores in the material. Again, these observations are consistent with previous studies in clay [17, 20]. Finally, the sample with abundant kaolinite clay showed a hysteresis loop but with a very small-sized envelope (Fig. 5d). The narrow gap implies nearly complete desorption and may infer the pore-scale homogeneity [52]. In other words, the kaolinite-rich material has larger pores and as substantiated from the size distribution. The interesting characteristic is the vertically narrow shape that resembles type H1 loop, nevertheless does not exhibit a plateau at high  $p/p^o$ . This feature matches type H3 loop or slit-shaped/macropores.

Forced closure of the desorption branch is seen in Fig. 5a, b and d at  $p/p^o \sim 0.44$ , and it is called the ‘Tensile Strength Effect’ due to the instability of the hemispherical meniscus during desorption in pores with critical diameters of approximately 4 nm (mesopores) [53]. It is noteworthy that the volume of adsorbed nitrogen displayed in Fig. 5 was measured at standard temperature (0 °C) and pressure (14.7 psi), above the two-phase critical temperature of N<sub>2</sub> (-147 °C). Since, gas expands and its volume increases with temperature, the volume at STP is expected to be higher than the volume at -196 °C, the condition at which the pore attributes were assessed. The actual pore structure characterization at a temperature of 77.4 K will be discussed in Sect. 3.4.

### 3.4 BJH Pore Size Distributions (PSDs)

The Kelvin-based N<sub>2</sub>-BJH technique is reliable in the description of the capillary condensation phenomenon in cylindrical pores [54], to accurately obtain the mesopores’ average sizes and pore distribution. However, the Gurwitsch rule assumptions of cylindrical and homogeneous pore geometry could limit the model’s reliability. This premise is partially correct in this study, as the hysteresis curves confirm the presence of cylindrical-shaped pores to some degree depending on the clay types. Furthermore, the BJH pore distribution (PSD) data was verified with observations from the SEM. The challenge is accurately computing the pore volume evaluated at 77 K across the pore-scales ranges.

The area under the N<sub>2</sub>-BJH differential volume distribution (Fig. 7) showed that mesopores and macropores contribute significantly to the total volume available in studied samples. Nevertheless, kaolinite has the highest distribution of large pores, followed by montmorillonite and chlorite. Aside from kaolinite-enriched rock, the differential volume of other clay samples reaches the peak and starts to decline. This limiting distribution means that the 2–50 nm volume capacity available in the materials is well characterized. There is a notable contribution of mesopores to the total volume capacity, and the amount of pore volume above 50 nm will be large in kaolinite compared to the three samples.



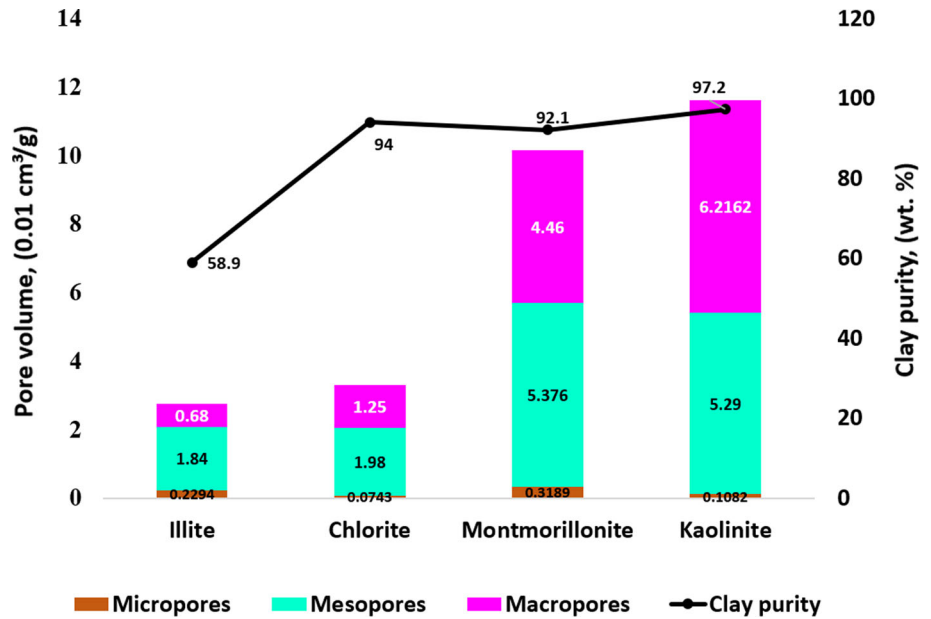
**Fig. 7** The BJH pore distribution obtained by inversion of N<sub>2</sub> gas adsorption data at 77 K. **a** Chlorite, **b** illite, **c** kaolinite, **d** montmorillonite

Figure 8 shows a direct relationship between the cumulative pore volume and clay purity. Kaolinite has the highest capacity to host fluid due to the significant mesopores and macropores followed by montmorillonite, chlorite and least in illite clay. The volume of 2–50 nm is highest in montmorillonite/kaolinite and least in illite. Kaolinite has the largest macropores volume and illite is the least. This observation is also confirmed by the Wang 2020 study [20]. Meanwhile, the mesopores volume fraction is the least in kaolinite abundant rock.

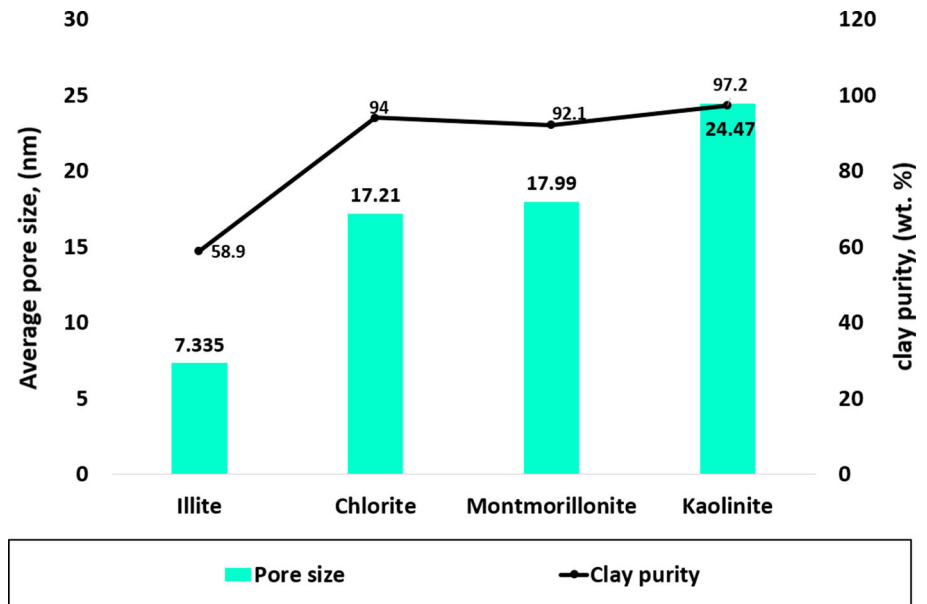
Figure 9 showed that the rock containing the highest clay purity has the largest average pore size, while the least amount of the element has the least average compartment sizes. However, the average pore size computed with the adsorption data will underestimate the volume of > 50 nm pores present in the layered phyllosilicate structure, since the N<sub>2</sub>-BJH model did not capture wider macropores (only 50–300 nm). The role of the clay chemical composition on the pore attributes evolution, gas storage, and production will be interesting to consider at typical reservoir pressure and temperature conditions.

Ultimately, the type of clay present in shale and their relative elemental concentration significantly affect the storage capacity and gas production. Several adsorption experiments compute the sorbed and free gas capacity in pure clay or clay-rich shale rocks at high pressure [39, 55]. However, the capacity of the clay materials to host fluid at high pressure has not been connected with their elemental concentration and clay purity. A similar pattern is expected with the adsorption of nitrogen at low-pressure STP. The limitation of the BJH N<sub>2</sub> adsorption model remains that it can only resolve the minimum pore size of approximately 1.7 nm, and the nitrogen probe is diffusion restricted in narrow micropores (< 0.7 nm). CO<sub>2</sub> adsorption at 273.15 K [20, 56] and Harkins and Jura t-plot [57] are commonly employed in the literature for characterizing materials with significant micropores.

**Fig. 8** The relationship between the clay minerals and pore volumes contribution from macropores, mesopores, and micropores in clay-rich samples with a pore size range of  $50 < d \leq 300$ ,  $2 \leq d \leq 50$ , and  $0.4 < d \leq 2\text{nm}$  respectively, evaluated at 77 K



**Fig. 9** The average pore size connection with clay purity in wt. %. The measurement in this study pore using the BJH method considered the distribution of 1.7–300 nm, while the average pore falls within the mesopore-scale at 77 K



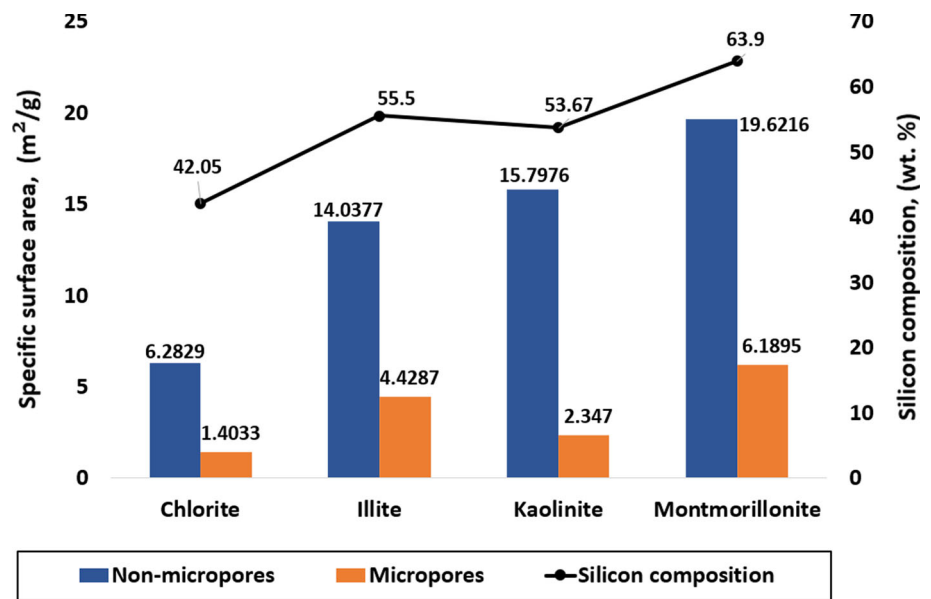
### 3.5 Micropores and Non-Micropores Specific Surface Area

The relationship between the silicon concentration and specific surface area is provided in Fig. 10. The specific surface area in non-micropores is referred to as the external SSA of the clay. Montmorillonite has the highest value, and chlorite contains the least. This trend is similar to the total specific surface area reported in the literature. The high SSA in non-micropores of the montmorillonite is coming from

the edge and basal-specific surface area contributions. However, care must be taken to understand that the total SSA using the  $\text{N}_2$  probe does not access the  $< 2.0$  nm interlayer spaces, even in swelling clay minerals like montmorillonite and chlorite. Regardless, the SSA of illite and kaolinite are reliable as they are non-swelling and their microstructure will be unchanged if the sample is wet [58, 59]. Also, the relatively large volume and specific surface area of micropores in montmorillonite as shown in Fig. 9, is consistent with the outcome of Wang's studies [20]. Finally, in the same vein, the micropores and non-micropores specific surface areas are in



**Fig. 10** The relationship between the micropores and non-micropores specific surface area in clay and the amount of silicon present evaluated at 77 K



descending order: montmorillonite > kaolinite > illite > chlorite clay-rich samples. Finally, the clays purity, aluminum and silicon concentration, specific surface area, average pore size, TOC and pore volume at all pore-scales are presented in Table 3.

#### 4 Implications of Using Aluminum and Silica-Rich Clay

Figure 2 and Table 3 show a direct association between the aluminum content and clay purity. Kaolinite clay has the highest aluminum concentration of 39.5 wt.% compared to chlorite, montmorillonite and illite with 23.0, 17.9 and 14.7 wt.%, respectively. Figures 6, 8, and 9 revealed the connection that unites the clay wt.% and its pore structural attributes such as the total pore volume, non-micropore volume and average pore sizes, respectively. A combined analysis of all the stated figures suggests that the capacity of clay to host fluids is enhanced by the concentration of aluminum present in the clay. This information is suitable for a meaningful understanding of the storage capacity of clay-rich shale plays depending on the clay types.

Additionally, the presence of aluminum in a material could cause an acceleration of surface reactivity [60] and serve as a reactant in the treatment of contaminants in polluted areas [61, 62]. Fatimah and Wijaya [60] study substantiated that the increase in the quantity of aluminum in montmorillonite clay speeds up the surface acidity reaction. Furthermore, Yang et al. [61] and Wang et al. [62] confirmed that an aluminum modified clay is applicable for phosphate and contaminant removal in polluted areas in the absence of air.

At this point, it is clear from this research that kaolinite-rich clay (with the highest aluminum concentration of 39.5 wt.%) has the potential to act as a good catalytic material required to speed up esterification reaction. In addition, it can serve as a waste repository and a material for the treatment of phosphorus-containing contaminants in polluted areas.

The relationship between silicon content and clay structural properties was also studied. Montmorillonite (63.9 wt.%) has the highest amount of silicon followed by illite (55.5 wt.%), kaolinite (53.7 wt.%), and chlorite (42.05 wt.%) in this order. The increase in this crystal-like mineral favors the development of the specific surface area in the non-micropores. Studies have shown the significance of silicon in clay research [63, 64]. Depending on the clay type, the presence of silica in clay can reduce the repulsive double-layer forces and, at the same time improve the attractive force between the replaced interlayer cation and clay surface. This phenomenon increases stabilization and reduces pore throat plugging in clay-rich shale [63]. Sadek [64] has also supported the observation that silica nanoparticles prepared at 200 °C contain macropores structure. However, these studies considered the use of silicon in pure form. Silicon in clay exists as an impure form. The existence of silica in sandstone increases the volume of macropores attributed to the high porosity in silicate-rich rocks [5]. In addition to the role of surface charge density on the clay-specific surface area [65], the concentration by wt.% of silica in clay was one of the surface area controlling factors. This research confirms that montmorillonite with the largest specific surface area in non-micropores and silicon content of 63.9 wt.% promotes reactivity and cation exchange interaction. However, this property of high basal spacing will prompt clay swelling in the presence of water [66].

**Table 3** Summary of BJH adsorption, BET, and t-plot method for characterizing clay pore volume, average pore size, total surface and external specific surface area versus elemental concentration and clay purity

Sample ID	Clay, wt. %	Al, wt. %	Si, wt. %	BET $S_{\text{tot}}$ , $\text{m}^2/\text{g}$	BJH adsorption (Micropores 1.7–2 nm, Mesopores 2–50 nm, Macropores 50–300 nm, and Total pores 1.7–300 nm)			Harkins and Jura t-plot (Micropores 0.4–2 nm)				
					$d_{\text{avg}}$ , nm	$V_{\text{tot}}$ , $0.01\text{cm}^3/\text{g}$	$V_{\text{mic}}$ , $0.01\text{cm}^3/\text{g}$	$V_{\text{mes}}$ , $0.01\text{cm}^3/\text{g}$	$V_{\text{mac}}$ , $0.01\text{cm}^3/\text{g}$	$S_{\text{mic}}$ , $\text{m}^2/\text{g}$	$S_{\text{ext}}$ , $\text{m}^2/\text{g}$	$V_{\text{mic}}$ , $0.01\text{cm}^3/\text{g}$
Montmorillonite	92.1	17.90	63.90	25.80	18.00	9.90	0.98	5.38	4.46	6.19	19.62	0.32
Kaolinite	97.20	39.50	55.70	18.10	24.50	11.50	0.03	5.29	6.22	2.35	15.80	0.11
Illite	58.90	14.70	55.50	18.50	7.30	2.60	0.11	1.84	0.68	4.43	14.04	0.23
Chlorite	94.00	23.00	42.10	7.70	17.20	3.30	0.04	1.98	1.25	1.40	6.28	0.07

## 5 Conclusions

In this research, four clay-rich rocks samples were characterized using an integrated approach to understand the relationship between aluminum, silicon concentration, clay purity and the intra-granular pore structural parameters. The combination of techniques such as  $\mu\text{XRF}$ , XRD, SEM–EDX, and low-temperature adsorption analyses showed some interesting relationship between their mineral's composition, specific surface area, pore distribution and volume. Furthermore, the following conclusions are drawn:

1. The results from mineralogy and elemental analyses showed that the studied samples with clay purities of 60–98% have a combined 80–96 wt.% composition of aluminum, silicon, and Iron. SEM backscattered electron image confirms the degree of sample clay homogeneity. Similarly, the SEM–EDS images validate the elemental analysis by  $\mu\text{XRF}$ .
2. Both the total organic content analysis and adsorption–desorption curve at  $p/p^o < 0.04$ , indicate that clays accommodate negligible micropores.
3. The inferred adsorption isotherm types hint that the materials contain a negligible amount of micropores and may be undergoing some pore-blocking phenomenon. Meanwhile, the hysteresis loop implies that clay has a plate-like/larger pore system. This observation is consistent in all the analyzed samples. Nevertheless, the pore shape complexity depends on the clay type.
4. Capillary condensation and evaporation curves revealed more mesopores and macropores of 2–50 nm and > 50 nm, respectively. The pore distribution plateaued around an average of 100 nm. The limiting distribution confirmed the suitability of the Barrett-Joyner-Halenda technique to compute most of the fluid volume contained in clay mesopores.
5. Kaolinite (74.43  $\text{cm}^3/\text{g}$ ) hosts the highest amount of  $\text{N}_2$  adsorbed at STP followed by montmorillonite (65.08  $\text{cm}^3/\text{g}$ ), chlorite (21.01  $\text{cm}^3/\text{g}$ ) and illite (16.59  $\text{cm}^3/\text{g}$ ) has the least capacity. In the same vein, the pore capacity to store fluid and average pore size assessed at 77.4 K follow a similar pattern and increase with aluminum and clay contents.
6. On the other hand, the specific surface area of the non-micropores is directly related to silicon composition. Montmorillonite with the largest specific surface area in non-micropores has a silicon content of 63.9 wt.%.
7. The novelty of linking elemental composition and intra-granular pore attributes in this study can be utilized to develop synthetic clay materials with improved surface and pore volume properties for waste treatment and catalyst for accelerating chemical reactions.



**Acknowledgements** The authors acknowledge the provision of experimental equipment by the College of Petroleum Engineering and Geosciences (CPG) and the Research Institute at King Fahd University of Petroleum and Minerals, Dhahran, Saudi Arabia. A special appreciation to Dr. Abduljamiu Olalekan Amao, Mr. Bandar Al-Otaibi, Ms. Mashaer Alfaraj, and Mr. Nadeem Syed for their assistance in CPG laboratory analyses. The authors thank Mr. Reynante Balmes Pagcaliwagan for his cooperation in using the Surface Area and Porosity analyzer Micromeritics ASAP2020 model for the N<sub>2</sub> adsorption experiment. The authors also thank anonymous reviewers for providing comments, which improve the manuscript's quality.

## Declarations

**Conflict of interest** The authors declare no competing financial interest.

## References

1. Yaalon, D.H.: Mineral composition of the average shale. *Clay Miner.* (1962). <https://doi.org/10.1180/claymin.1962.5.27.05>
2. Ambrose, R.J.; Hartman, R.C.; Diaz-Campos, M.; Akkutlu, I.Y.; Sondergeld, C.H.: Shale gas-in-place calculations. Part I: new pore-scale considerations. *SPE J.* **17**, 219–229 (2012). <https://doi.org/10.2118/131772-PA>
3. Afagwu, C.; Abubakar, I.; Kalam, S.; Al-Afnan, S.F.; Awotunde, A.A.: Pressure-transient analysis in shale gas reservoirs: a review. *J. Nat. Gas Sci. Eng.* **78**, 103319 (2020). <https://doi.org/10.1016/j.jngse.2020.103319>
4. Jin, Z.; Firoozabadi, A.: Methane and carbon dioxide adsorption in clay-like slit pores by Monte Carlo simulations. *Fluid Phase Equilib.* **360**, 456–465 (2013). <https://doi.org/10.1016/j.fluid.2013.09.047>
5. Ross, D.J.K.; Marc-Bustin, R.: The importance of shale composition and pore structure upon gas storage potential of shale gas reservoirs. *Mar. Pet. Geol.* **26**, 916–927 (2009). <https://doi.org/10.1016/j.marpetgeo.2008.06.004>
6. Yuan, Y.; Rezaee, R.: Comparative porosity and pore structure assessment in shales: measurement techniques, influencing factors and implications for reservoir characterization. *Energies* **12**, 7–9 (2019). <https://doi.org/10.3390/en12112094>
7. Zhang, Y.; Shao, D.; Yan, J.; Jia, X.; Li, Y.; Yu, P.; Zhang, T.: The pore size distribution and its relationship with shale gas capacity in organic-rich mudstone of Wufeng-Longmaxi Formations, Sichuan Basin, China. *J. Nat. Gas Geosci.* **1**, 213–220 (2016). <https://doi.org/10.1016/j.jnggs.2016.08.002>
8. El Ouahabi, M.; Daoudi, L.; Fagel, N.: Mineralogical and geotechnical characterization of clays from northern Morocco for their potential use in the ceramic industry. *Clay Miner.* (2014). <https://doi.org/10.1180/claymin.2014.049.1.04>
9. Hubert, F.; Caner, L.; Meunier, A.; Lanson, B.: Advances in characterization of soil clay mineralogy using X-ray diffraction: from decomposition to profile fitting. *Eur. J. Soil Sci.* **60**, 1093–1105 (2009). <https://doi.org/10.1111/j.1365-2389.2009.01194.x>
10. Środoń, J.: Chapter 12.2 identification and quantitative analysis of clay minerals. *Dev. Clay Sci.* **1**, 765–787 (2006). [https://doi.org/10.1016/S1572-4352\(05\)01028-7](https://doi.org/10.1016/S1572-4352(05)01028-7)
11. Mattioli, M.; Giardini, L.; Roselli, C.; Desideri, D.: Mineralogical characterization of commercial clays used in cosmetics and possible risk for health. *Appl. Clay Sci.* **119**, 449–454 (2016). <https://doi.org/10.1016/j.clay.2015.10.023>
12. Zhong, H.; Yang, T.; Yin, H.; Lu, J.; Zhang, K.; Fu, C.: Role of Alkali type in chemical loss and ASP-flooding enhanced oil recovery in Sandstone formations. *SPE Reserv. Eval. Eng.* **23**, 431–445 (2020). <https://doi.org/10.2118/191545-PA>
13. Zhao, Y.; Han, C.; Sun, Y.; Danesh, N.N.; Liu, T.; Gao, Y.: Nano-to micro-pore characterization by synchrotron radiation SAXS and nano-CT for bituminous coals. *Front. Earth Sci.* **15**, 189–201 (2021). <https://doi.org/10.1007/s11707-021-0889-6>
14. Loucks, R.G.; Reed, R.M.; Ruppel, S.C.; Jarvie, D.M.: Morphology, genesis, and distribution of nanometer-scale pores in siliceous mudstones of the Mississippian Barnett Shale. *J. Sediment. Res.* **79**, 848–861 (2009). <https://doi.org/10.2110/jsr.2009.092>
15. Tang, Y.; Hou, C.; He, Y.; Wang, Y.; Chen, Y.; Rui, Z.: Review on pore structure characterization and microscopic flow mechanism of CO<sub>2</sub> flooding in porous media. *Energy Technol.* **2021**, 9 (2021). <https://doi.org/10.1002/ente.202000787>
16. Aringhieri, R.: Nanoporosity characteristics of some natural clay minerals and soils. *Clays Clay Miner.* (2004). <https://doi.org/10.1346/CCM.2004.0520604>
17. Luo, P.; Zhong, N.; Khan, I.; Wang, X.; Wang, H.; Luo, Q.; Guo, Z.: Effects of pore structure and wettability on methane adsorption capacity of mud rock: insights from mixture of organic matter and clay minerals. *Fuel* **251**, 551–561 (2019). <https://doi.org/10.1016/j.fuel.2019.04.072>
18. Kuila, U.; Prasad, M.: Specific surface area and pore-size distribution in clays and shales. *Geophys. Prospect.* (2013). <https://doi.org/10.1111/1365-2478.12028>
19. Tompsett, G.A.; Krogh, L.; Griffin, D.W.; Conner, W.C.: Hysteresis and scanning behavior of mesoporous molecular sieves. *Langmuir* **21**, 8214–8225 (2005). <https://doi.org/10.1021/la050068y>
20. Wang, X.; Cheng, H.; Chai, P.; Bian, J.; Wang, X.; Liu, Y.; Yin, X.; Pan, S.; Pan, Z.: Pore characterization of different clay minerals and its impact on methane adsorption capacity. *Energy Fuels* **34**, 12204–12214 (2020). <https://doi.org/10.1021/acs.energyfuels.0c01922>
21. Sayed Hassan, M.; Villieras, F.; Gaboriaud, F.; Razaftianamaharavo, A.: AFM and low-pressure argon adsorption analysis of geometrical properties of phyllosilicates. *J. Colloid Interface Sci.* **296**, 614–623 (2006). <https://doi.org/10.1016/j.jcis.2005.09.028>
22. Macht, F.; Eusterhues, K.; Pronk, G.J.; Totsche, K.U.: Specific surface area of clay minerals: comparison between atomic force microscopy measurements and bulk-gas (N<sub>2</sub>) and -liquid (EGME) adsorption methods. *Appl. Clay Sci.* **53**, 20–26 (2011). <https://doi.org/10.1016/j.clay.2011.04.006>
23. Kariem, H.; Kiefer, T.; Hellmich, C.; Gaggl, W.; Steiger-Thirsfeld, A.; Füssl, J.: EDX/XRD-based identification of micrometer-sized domains in scanning electron micrographs of fired clay. *Mater. Struct. Constr.* **2020**, 53 (2020). <https://doi.org/10.1617/s11527-020-01531-7>
24. Ochieng, O.: Characterization and classification of clay minerals for potential applications in Rugi Ward, Kenya. *Afr. J. Environ. Sci. Technol.* (2016). <https://doi.org/10.5897/ajest2016.2184>
25. Adeniyi, F.I.; Ogundiran, M.B.; Hemalatha, T.; Hanumantra, B.B.: Characterization of raw and thermally treated Nigerian kaolinite-containing clays using instrumental techniques. *SN Appl. Sci.* **2**, 1–14 (2020). <https://doi.org/10.1007/s42452-020-2610-x>
26. Chen, J.J.; Sorelli, L.; Vandamme, M.; Ulm, F.J.; Chanvillard, G.: A coupled nanoindentation/SEM-EDS study on low water/cement ratio portland cement paste: evidence for C-S-H/Ca(OH)<sub>2</sub> nanocomposites. *J. Am. Ceram. Soc.* **93**, 1484–1493 (2010). <https://doi.org/10.1111/j.1551-2916.2009.03599.x>
27. Boulingui, J.E.; Nkoumbou, C.; Njoya, D.; Thomas, F.; Yvon, J.: Characterization of clays from Mezafe and Mengono (Ne-Libreville, Gabon) for potential uses in fired products. *Appl. Clay Sci.* **115**, 132–144 (2015). <https://doi.org/10.1016/j.clay.2015.07.029>
28. Zaffar, M.; Lu, S.G.: Pore size distribution of clayey soils and its correlation with soil organic matter. *Pedosphere* **25**, 240–249 (2015). [https://doi.org/10.1016/S1002-0160\(15\)60009-1](https://doi.org/10.1016/S1002-0160(15)60009-1)



29. Li, W.; Lu, S.; Xue, H.; Zhang, P.; Hu, Y.: Microscopic pore structure in shale reservoir in the argillaceous dolomite from the Jiangnan Basin. *Fuel* **181**, 1041–1049 (2016). <https://doi.org/10.1016/j.fuel.2016.04.140>
30. Wilson, W.; Sorelli, L.; Tagnit-Hamou, A.: Automated coupling of NanoIndentation and quantitative energy-dispersive spectroscopy (NI-QEDS): a comprehensive method to disclose the micro-chemo-mechanical properties of cement pastes. *Cem. Concr. Res.* **103**, 49–65 (2018). <https://doi.org/10.1016/j.cemconres.2017.08.016>
31. Elgamouz, A.; Tijani, N.; Shehadi, I.; Hasan, K.; Al-Farooq Kawam, M.: Characterization of the firing behaviour of an illite-kaolinite clay mineral and its potential use as membrane support. *Heliyon*. **5**, e02281 (2019). <https://doi.org/10.1016/j.heliyon.2019.e02281>
32. Qian, G.; Li, Y.; Gerson, A.R.: Applications of surface analytical techniques in earth sciences (2015)
33. Lei, Q.; Zhang, L.; Tang, H.; Zhao, Y.; Chen, M.; Xie, C.: Describing the full pore size distribution of tight sandstone and analyzing the impact of clay type on pore size distribution. *Geofluids* (2020). <https://doi.org/10.1155/2020/5208129>
34. Kamal, M.S.; Mahmoud, M.; Hanfi, M.; Elkhatny, S.; Hussein, I.: Clay minerals damage quantification in sandstone rocks using core flooding and NMR. *J. Pet. Explor. Prod. Technol.* **9**, 593–603 (2019). <https://doi.org/10.1007/s13202-018-0507-7>
35. Takkiri-Borujeni, A.; Kazemi, M.; Sun, T.; Mansouri-Boroujeni, M.: Effect of kerogen type and maturity on performance of carbon dioxide storage in shale. In: *Proc. SPE Annu. Tech. Conf. Exhib.* 2040 (2017). <https://doi.org/10.2118/187360-ms>
36. Obliger, A.; Ulm, F.J.; Pellenq, R.: Impact of nanoporosity on hydrocarbon transport in shales' organic matter. *Nano Lett.* **18**, 832–837 (2018). <https://doi.org/10.1021/acs.nanolett.7b04079>
37. Vandenbroucke, M.; Largeau, C.: Kerogen origin, evolution and structure. *Org. Geochem.* **38**, 719–833 (2007). <https://doi.org/10.1016/j.orggeochem.2007.01.001>
38. Okiongbo, K.S.; Aplin, A.C.; Larter, S.R.: Changes in type II Kerogen density as a function of maturity: evidence from the Kimmeridge clay formation. *Energy Fuels* **19**, 2495–2499 (2005). <https://doi.org/10.1021/ef050194+>
39. Ji, L.; Zhang, T.; Milliken, K.L.; Qu, J.; Zhang, X.: Experimental investigation of main controls to methane adsorption in clay-rich rocks. *Appl. Geochem.* **27**, 2533–2545 (2012). <https://doi.org/10.1016/j.apgeochem.2012.08.027>
40. Dang, W.; Zhang, J.; Wei, X.; Tang, X.; Chen, Q.; Li, Z.; Zhang, M.; Liu, J.: Geological controls on methane adsorption capacity of Lower Permian transitional black shales in the Southern North China Basin, Central China: experimental results and geological implications. *J. Pet. Sci. Eng.* **152**, 456–470 (2017). <https://doi.org/10.1016/j.petrol.2017.03.017>
41. Amao, A.O.; Al-Ramadan, K.; Koeshidayatullah, A.: Automated mineralogical methodology to study carbonate grain microstructure: an example from oncoids. *Environ. Earth Sci.* **75**, 1–11 (2016). <https://doi.org/10.1007/s12665-016-5492-x>
42. Afagwu, C.; Mahmoud, M.A.; Alafnan, S.; Patil, S.: Multiscale storage and transport modeling in unconventional shale gas: a review. *J. Pet. Sci. Eng.* **2021**, 109518 (2021). <https://doi.org/10.1016/j.petrol.2021.109518>
43. Brunauer, S.; Emmett, P.H.; Teller, E.: Adsorption of gases in multimolecular layers. *J. Am. Chem. Soc.* **60**, 309–319 (1938). <https://doi.org/10.1021/ja01269a023>
44. Sing, K.: The use of nitrogen adsorption for the characterization of porous materials. *Colloids Surfaces A Physicochem. Eng. Asp.* **187–188**, 3–9 (2001). [https://doi.org/10.1016/S0927-7757\(01\)00612-4](https://doi.org/10.1016/S0927-7757(01)00612-4)
45. Mohammed, I.; Afagwu, C.C.; Adjei, S.; Kadafur, I.B.; Jamal, M.S.; Awotunde, A.A.: A review on polymer, gas, surfactant and nanoparticle adsorption modeling in porous media. *Oil Gas Sci. Technol.* **2020**, 75 (2020). <https://doi.org/10.2516/ogst/2020063>
46. Tian, H.; Pan, L.; Zhang, T.; Xiao, X.; Meng, Z.; Huang, B.: Pore characterization of organic-rich Lower Cambrian shales in Qiannan Depression of Guizhou Province, Southwest China. *Mar. Pet. Geol.* **62**, 28–43 (2015). <https://doi.org/10.1016/j.marpetgeo.2015.01.004>
47. Rouquerol, J.; Llewellyn, P.; Rouquerol, F.: Is the BET equation applicable to microporous adsorbents? *Stud. Surf. Sci. Catal.* (2007). [https://doi.org/10.1016/s0167-2991\(07\)80008-5](https://doi.org/10.1016/s0167-2991(07)80008-5)
48. de Boer, J.H.; Lippens, B.C.; Linsen, B.G.; Broekhoff, J.C.P.; van den Heuvel, A.; Osinga, T.J.: Thet-curve of multimolecular N<sub>2</sub>-adsorption. *J. Colloid Interface Sci.* **21**, 405–414 (1966). [https://doi.org/10.1016/0095-8522\(66\)90006-7](https://doi.org/10.1016/0095-8522(66)90006-7)
49. Coasne, B.; Gubbins, K.E.; Pellenq, R.J.M.: A Grand Canonical Monte Carlo study of adsorption and capillary phenomena in nanopores of various morphologies and topologies: testing the BET and BJH characterization methods. *Part. Part. Syst. Charact.* **21**, 149–160 (2004). <https://doi.org/10.1002/ppsc.200400928>
50. Sing, K.S.W.: Reporting physisorption data for gas/solid systems. Presented at the (1984)
51. Xiong, J.; Liu, X.; Liang, L.; Zeng, Q.: Adsorption of methane in organic-rich shale nanopores: an experimental and molecular simulation study. *Fuel* **200**, 299–315 (2017). <https://doi.org/10.1016/j.fuel.2017.03.083>
52. Barsotti, E.; Tan, S.P.; Piri, M.; Chen, J.H.: Capillary-condensation hysteresis in naturally-occurring nanoporous media. *Fuel* **2020**, 263 (2020). <https://doi.org/10.1016/j.fuel.2019.116441>
53. Groen, J.C.; Peffer, L.A.A.; Pérez-Ramírez, J.: Pore size determination in modified micro- and mesoporous materials. Pitfalls and limitations in gas adsorption data analysis. *Microporous Mesoporous Mater.* **60**, 1–17 (2003). [https://doi.org/10.1016/S1387-1811\(03\)00339-1](https://doi.org/10.1016/S1387-1811(03)00339-1)
54. Barrett, E.P.; Joyner, L.G.; Halenda, P.P.: The determination of pore volume and area distributions in porous substances. I. Computations from nitrogen isotherms. *J. Am. Chem. Soc.* (1951). <https://doi.org/10.1021/ja01145a126>
55. Hwang, J.; Pini, R.: Supercritical CO<sub>2</sub> and CH<sub>4</sub> uptake by illite-smectite clay minerals. *Environ. Sci. Technol.* **53**, 11588–11596 (2019). <https://doi.org/10.1021/acs.est.9b03638>
56. Li, T.; Tian, H.; Chen, J.; Cheng, L.: Application of low pressure gas adsorption to the characterization of pore size distribution of shales: an example from Southeastern Chongqing area, China. *J. Nat. Gas Geosci.* **1**, 221–230 (2016). <https://doi.org/10.1016/j.jnggs.2016.07.001>
57. Tian, H.; Li, T.; Zhang, T.; Xiao, X.: Characterization of methane adsorption on overmature Lower Silurian-Upper Ordovician shales in Sichuan Basin, southwest China: experimental results and geological implications. *Int. J. Coal Geol.* **156**, 36–49 (2016). <https://doi.org/10.1016/j.coal.2016.01.013>
58. Tournassat, C.; Bourg, I.C.; Steefel, C.I.; Bergaya, F.: Surface properties of clay minerals. *Dev. Clay Sci.* **6**, 5–31 (2015)
59. Muhammed, N.S.; Olayiwola, T.; Elkhatny, S.; Haq, B.; Patil, S.: Journal of Natural Gas Science and Engineering Insights into the application of surfactants and nanomaterials as shale inhibitors for water-based drilling fluid: a review. *J. Nat. Gas Sci. Eng.* **92**, 103987 (2021). <https://doi.org/10.1016/j.jngse.2021.103987>
60. Fatimah, I.; Narsito, W.K.: Effect of aluminium content in aluminium pillared montmorillonite on its surface acidity properties. *ITB J. Sci.* **43**(A), 123–138 (2011). <https://doi.org/10.5614/itbj.sci.2011.43.2.5>
61. Yang, H.; He, K.; Lu, D.; Wang, J.; Xu, D.; Jin, Z.; Yang, M.; Chen, J.: Removal of phosphate by aluminum-modified clay in a heavily polluted lake, Southwest China: effectiveness and ecological risks. *Sci. Total Environ.* **705**, 135850 (2020). <https://doi.org/10.1016/j.scitotenv.2019.135850>



62. Wang, J.; Chen, J.; Chen, Q.; Yang, H.; Zeng, Y.; Yu, P.; Jin, Z.: Assessment on the effects of aluminum-modified clay in inactivating internal phosphorus in deep eutrophic reservoirs. *Chemosphere* **215**, 657–667 (2019). <https://doi.org/10.1016/j.chemosphere.2018.10.095>
63. Roshan, H.; Lv, A.; Aghighi, M.A.; Sarmadivaleh, M.; Siddiqui, M.A.Q.; van As, D.; Ehsani, S.: Stabilization of clay-rich interburdens using silica nanoparticles. *J. Pet. Sci. Eng.* **211**, 110126 (2022). <https://doi.org/10.1016/j.petrol.2022.110126>
64. Sadek, O.M.; Reda, S.M.; Al-Bilali, R.K.: Preparation and characterization of silica and clay-silica core-shell nanoparticles using sol-gel method. *Adv. Nanoparticl.* (2013). <https://doi.org/10.4236/anp.2013.22025>
65. Alperovitch, N.; Shainberg, I.; Keren, R.; Singer, M.J.: Effect of clay mineralogy and aluminium and iron oxides on the hydraulic conductivity of clay-sand mixtures. *Clays Clay Miner.* (1985). <https://doi.org/10.1346/ccmn.1985.0330511>
66. Muhammed, N.S.; Olayiwola, T.; Elkatatny, S.: A review on clay chemistry, characterization and shale inhibitors for water-based drilling fluids. *J. Pet. Sci. Eng.* **206**, 109043 (2021)

